

# Overstability of Lamellar Eutectic Growth below the Minimum-Undercooling Spacing

S. AKAMATSU, M. PLAPP, G. FAIVRE, and A. KARMA

We investigate the stability of lamellar eutectic growth by thin-sample directional solidification experiments and two-dimensional phase-field simulations. We find that lamellar patterns can be morphologically stable for spacings smaller than the minimum undercooling spacing  $\lambda_m$ . Key to this finding is the direct experimental measurement of the relationship between the front undercooling and spacing, which identifies  $\lambda_m$  independently of the Jackson and Hunt (JH) theory and of uncertainties of alloy parameters. This finding conflicts with the common belief that patterns with  $\lambda < \lambda_m$  should be unstable, which is based on the Jackson–Hunt–Cahn assumption that lamellae grow normal to the envelope of the front. Our simulation results reveal that lamellae also move parallel to this envelope to reduce spacing gradients, thereby weakly violating this assumption but strongly overstabilizing patterns for a range of spacing below  $\lambda_m$  that increases with  $G/V$  (temperature gradient to growth rate ratio). This range is much larger than predicted by previous stability analyses and can be significant for standard experimental conditions. An analytical expression is obtained phenomenologically, which predicts well the variation of the smallest stable spacing with  $G/V$ . We also present results that shed light on the history-dependent selection and long-time evolution of the experimentally observed range of spacings.

## I. INTRODUCTION

THE understanding and the control of solidification microstructures have been research subjects of both practical and fundamental interest for decades.<sup>[1]</sup> Much progress has been made, but our current knowledge still has important deficiencies. The control of the spacing ( $\lambda$ ) of directionally solidified lamellar eutectics is one of the long-standing problems that remain largely open today. A major difficulty—in this as in many other problems in solidification—is that features of the pattern such as the average value and spatial distribution of  $\lambda$  are initial-condition dependent. At fixed parameters of a directional-solidification experiment (physical constants and composition of the alloy, pulling rate  $V$ , and applied thermal gradient  $G$ ), they depend on the entire history of the sample, and in particular on the preparatory and initial stages of the solidification runs.<sup>[2,3]</sup> This follows from the highly nonlinear nature of the dynamical processes through which the microstructures appear. Such processes do not usually lead to a unique “selected” state.

Concerning the fundamental aspects of lamellar eutectic growth, the work of reference remains that of Jackson and Hunt (JH).<sup>[4]</sup> They showed that eutectics can be directionally solidified into a uniform lamellar microstructure, which is the trace left behind in the solid by a steady-state periodic nonlinear growth pattern (Figure 1). Most importantly, they established theoretically that, at fixed  $V$ , such a pattern can exist for any value of a wide range of

spacings. This prediction has been confirmed theoretically and experimentally.<sup>[5,6,7]</sup>

The existence of a wide range of possible spacings raises the question of the stability of these patterns as a function of  $\lambda$ . The large  $\lambda$  stability limit has been the subject of many studies in recent years.<sup>[5,6,7]</sup> It was found that the relevant instabilities are period-preserving or period-doubling oscillations appearing above a critical spacing, which depends on the alloy phase diagram and composition.

Here, we focus on the stability limit for small spacings. With regard to this question, Jackson and Hunt made a conjecture based on the particular shape of the dependence on  $V$  and  $\lambda$  of the average front undercooling  $\Delta T \equiv T_E - T_{av}$ , where  $T_E$  is the eutectic temperature and  $T_{av}$  the average temperature of the front, which can be obtained from the position of the (planar) envelope  $\bar{\zeta}(x)$  of the pattern along the growth axis  $z$  (Figure 2). The relation between  $\Delta T$ ,  $V$ , and  $\lambda$  reads in the JH approximation:

$$\Delta T(\lambda, V) = K_1 V \lambda + K_2 / \lambda \quad [1]$$

where  $K_1$  and  $K_2$  are functions of the physical constants and the concentration  $C$  of the (binary) alloy.<sup>[8]</sup> The first term on the right-hand side of Eq. [1] originates from the inter-lamellar diffusion field, and the second from the surface tensions of the solid-liquid and solid-solid interfaces. A particular feature of the  $\Delta T(\lambda)$  curve for fixed  $V$  is that it passes through a minimum at a value  $\lambda_m = \sqrt{K_1/K_2} V^{-1/2}$ , called the minimum-undercooling spacing. The formula [1], which was established for a spatially uniform steady-state pattern, holds true for any smooth spatial variation of  $\lambda$ . This means that, due to the presence of the temperature gradient, a spacing variation is inseparable from a deformation of the front envelope. If one assumes that the lamellae are constrained to grow normal to the envelope of the front, the stationary patterns are unstable for  $\lambda$  smaller than  $\lambda_m$ ; the spatial modulations of  $\lambda$  are amplified, which ultimately leads to lamella elimination (Figure 3). The main consequence of this

S. AKAMATSU, Associate Researcher, and G. FAIVRE, Senior Researcher, are with the Groupe de Physique des Solides, CNRS, and Universités Pierre-et-Marie-Curie and Denis-Diderot, 75015 Paris, France. Contact e-mail: akamatsu@gps.jussieu.fr M. PLAPP, Associate Researcher, is with the Laboratoire de Physique de la Matière Condensée, CNRS/Ecole Polytechnique, 91128 Palaiseau, France. A. KARMA, Professor, is with the Physic Department, Northeastern University, Boston, MA 02115.

Manuscript submitted August 7, 2003.

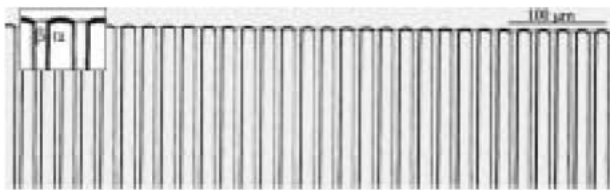


Fig. 1—Stationary lamellar-eutectic front of a nearly eutectic  $\text{CBr}_4\text{-C}_2\text{Cl}_6$  alloy ( $C \approx 11.6$  mol pct) in thin-sample directional solidification (in this micrograph, as in the following ones, the growth direction is upward) in a  $12\text{-}\mu\text{m}$ -thick sample.  $V = 0.5\text{ }\mu\text{m/s}$ ;  $G = 80\text{ K cm}^{-1}$ . Section III-A gives the characteristics of the alloy and the experimental setup.

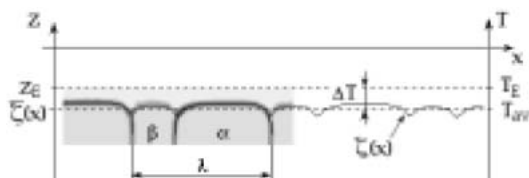


Fig. 2—Large-magnification micrograph of a steady-state lamellar pattern. Thin line: skeletonized shape  $\zeta(x)$  of the front. Refer to text for the definition of the symbols.

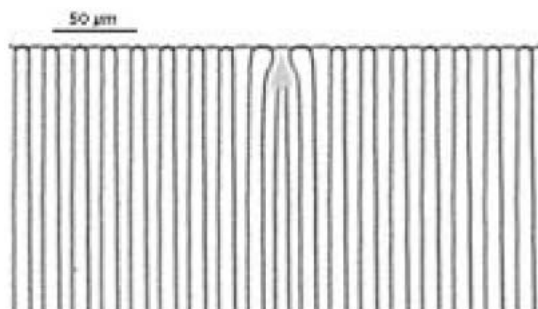


Fig. 3—Elimination of a lamella after a downward velocity jump from  $0.39\text{ }\mu\text{m s}^{-1}$  ( $\Lambda_0 \approx 0.81$ ) to  $0.26\text{ }\mu\text{m s}^{-1}$  ( $\Lambda_0 \approx 0.66$ ).  $C \approx 13.9$  mol pct;  $G = 80\text{ K cm}^{-1}$ .

normal-growth conjecture (which JH attributed to Cahn in their original article<sup>[4]</sup>), is that  $\lambda_m$  is the lower bound of the stability interval of steady-state lamellar eutectic patterns.

This argument, often called the minimum-undercooling conjecture, was later formalized by Langer<sup>[9]</sup> and Datye and Langer<sup>[10]</sup> through a stability analysis of the JH solution. Subsequently, this question has been addressed by a detailed analysis of the full nonlinear front equation in the limit of large temperature gradients  $G$ ,<sup>[12]</sup> and more recently by a multiple scale expansion method valid for arbitrary temperature gradients.<sup>[13]</sup> These studies showed that the lower stability limit is smaller than  $\lambda_m$ , but that the difference is negligibly small for the values of  $G$  that are used in standard directional solidification experiments.

Experimental studies of this issue have been scarce. In support of the minimum-undercooling conjecture, JH quoted several experimental facts including their own observations of lamella elimination events in thin samples of a transparent nonfaceted eutectic alloy ( $\text{CBr}_4\text{-C}_2\text{Cl}_6$ ), and the measurements made in many metallic eutectics showing that the average value of  $\lambda$  varies as  $V^{-1/2}$ , within experimental

uncertainty, and is of comparable magnitude to  $\lambda_m$  calculated from the physical constants of the alloy. These facts, alone, are not conclusive. The normal-growth conjecture certainly is a good approximation in some cases,<sup>[14]</sup> but its degree of inaccuracy has never been assessed under the conditions in which lamella elimination takes place. On the other hand, for all the studied eutectic alloys, the uncertainty on the materials constants and the scatter of the measurements of  $\lambda$  are far too large to permit a conclusion about the validity of the minimum-undercooling conjecture. In fact, the allegation that, in the experiments,  $\lambda$  scales as  $V^{-1/2}$  is questionable, especially at small values of  $V$ .<sup>[15]</sup> More importantly, the measured values of  $\lambda$  always show a strong (20 pct or more) dispersion, whatever the duration of the solidification run, suggesting that this dispersion is a permanent (non relaxing) feature of the growth pattern.<sup>[16]</sup> Previous experimental studies in thin-sample directional solidification of  $\text{CBr}_4\text{-C}_2\text{Cl}_6$  alloys gave insight into the latter fact.<sup>[7,14,17]</sup> The dispersion of  $\lambda$  was shown to be a combined effect of the physical inhomogeneities of the samples (mostly eutectic grain boundaries, as discussed subsequently), and the very long lifetime of the spatial modulations of  $\lambda$  when the bounds of these modulations are inside the stability range of the stationary patterns. These investigations, as well as the numerical studies by Karma and Sarkissian<sup>[6]</sup> suggested, but did not prove, that the lamella elimination threshold does not coincide with  $\lambda_m$ , but is usually smaller than this value.

In this article, we present a set of experimental and numerical results about the lamella elimination instability, which, to our knowledge, constitutes the first conclusive (and negative) test of the minimum-undercooling and normal-growth conjectures. As in previous studies, the experimental system is thin-sample directional solidification (TDS) of  $\text{CBr}_4\text{-C}_2\text{Cl}_6$  alloys. The reason for which we are now—and only now—able to achieve a critical experimental test of JH's conjectures can be easily explained. Except in its final stages (Figure 3), the lamella elimination process involves deformations of the front envelope whose amplitudes do not exceed a few tenths of a micron, and whose range extends over several hundreds of microns. The reliability of the TDS method (thermal and chemical stability) and the spatial sensitivity of numerical image processing methods have reached the level required for a spatiotemporal follow-up of such a process only recently. The numerical calculations are performed with a phase-field model and allow us to conduct a direct test of the normal-growth hypothesis.

The presentation of the results, in both experimental and numerical sections, is divided into two main parts. First, we study the response of lamellar eutectic patterns to long-range perturbations for values of  $\lambda$  ranging from  $\lambda_m$  to values much lower than  $\lambda_m$ , and determine the lamella elimination threshold  $\lambda_c$  as the limit separating stable from unstable patterns. Part of these results have already been published<sup>[18]</sup> but need to be repeated here for the sake of clarity. Experimentally speaking, the crucial point is that we are able to measure the  $\Delta T(\lambda)$  curve of the system *in situ*, thereby eliminating the usual uncertainties on the exact value of  $\lambda_m$  in the experiments. We find that  $\lambda_c$  is considerably lower than  $\lambda_m$  (typically,  $\lambda_c \approx 0.7\lambda_m$ ) in the experiments. The numerical simulations confirm this conclusion and give insight into the physical origin of this discrepancy between theoretical predictions and experimental results. The “overstability” of

lamellar eutectics with respect to the JH–Cahn theory is due to the breakdown of the normal-growth conjecture. The trijunction points, in addition to the conjectured normal motion, also show a slight lateral “sliding” motion in response to gradients of the local spacing. This leads to a smoothing of the spacing gradients, and hence opposes the destabilizing effect of the front deformations. From the simulation data, we obtain a phenomenological relationship between  $\lambda_c/\lambda_m$  and the control parameters. Remarkably, this relationship also describes well our experimental data, although the two alloy systems and the control parameters differ.

In a second part, we study the process of transformation of an unstable pattern (*i.e.*, a pattern of initial spacing  $\lambda_i$  smaller than  $\lambda_c$ ) to a stable one as a function of the distance from the instability threshold. We find two distinct typical scenarios. At low values of  $\lambda_c - \lambda_i$ , the lamella elimination instability first appears at some favorable spot of the front, and then propagates laterally at a constant speed. In the general theory of nonlinear phenomena, this is known as the propagation of a one-dimensional “front” or “wall” (we shall use this last term thereafter to avoid confusion with the growth front) into a linearly unstable state.<sup>[19,20]</sup> At larger values of  $\lambda_c - \lambda_i$ , the lamella elimination instability occurs almost simultaneously everywhere. Interestingly, we find that the final spacing delivered by either of these processes is close to  $\lambda_c$ , and thus smaller than  $\lambda_m$ , which implies that it varies with  $V$  less rapidly than  $V^{-1/2}$  for small  $V$ . This may have an impact on the interpretation of previous observations performed in metallic systems.

The remainder of the article is organized as follows. Section II outlines the theoretical background, and Section III contains some experimental details. The experimental results are presented in Section IV, while a brief description of the phase-field model and the numerical results are presented in Section V. The results are discussed in detail in Section VI; Section VII contains a brief conclusion.

## II. THEORETICAL BACKGROUND

We first briefly recall the stability analyses of thin lamellar eutectics of Langer<sup>[9]</sup> and Datye and Langer.<sup>[10]</sup> When the lamellar spacing varies slowly along the front,  $\partial_x \lambda \ll 1$ , (1) the envelope of the front, (2) the lateral displacements of the trijunction points with respect to their positions in a strictly periodic array of spacing  $\lambda_0$ , and (3) the spacing distribution may all be represented by slowly varying functions of  $x$  denoted here by  $\bar{\zeta}(x)$ ,  $y(x)$ , and  $\lambda(x)$ , respectively. These definitions imply that  $\lambda(x) \approx \lambda_0(1 + \partial_x \bar{\zeta})$ . Furthermore, the JH relation can be assumed to remain locally valid for a smoothly varying spacing, that is,  $\bar{\zeta}(x)G = -\Delta T[\lambda(x)]$ , with  $\Delta T$  given by Eq. [1]. Here, we have defined that  $\bar{\zeta} = 0$  corresponds to the isotherm at  $T_E$ . Cahn’s normal growth conjecture translates to  $\partial_t y(x) = -V \partial_x \bar{\zeta}$ . Combining all of the preceding relations, and linearizing the JH relation around the initial spacing  $\lambda_0$ , one obtains

$$\partial_t \lambda(x, t) = D_\lambda \partial_x^2 \lambda(x, t) \quad [2]$$

with  $D_\lambda = D_\perp$ ,

$$D_\perp = \frac{V \lambda_0}{G} \frac{d \Delta T(\lambda)}{d \lambda} \Big|_{\lambda=\lambda_0} = \frac{K_1 \lambda_0 V^2}{G} \left( 1 - \frac{1}{\Lambda_0^2} \right) \quad [3]$$

where we have defined the dimensionless spacing

$$\Lambda_0 \equiv \lambda_0 / \lambda_m \quad [4]$$

Equation [2] is generally referred to as the phase-diffusion equation in the pattern formation literature.<sup>[11]</sup> This terminology comes from expressing the complex amplitude of a long-wavelength modulation of a periodic pattern in a form  $\sim \exp[i\Phi(x, t)]$ , where the local gradient of the phase,  $\partial_x \Phi(x, t)$ , is inversely proportional to the local spacing of the pattern,  $\lambda(x, t)$ . The phase  $\Phi(x, t)$ , or equivalently  $\lambda(x, t)$ , obeys a diffusion equation that is ubiquitous in quasi-one-dimensional pattern forming systems whose governing equations are invariant under both translation ( $x \rightarrow x + x_0$ ) and parity ( $x \rightarrow -x$ ) symmetry, as is the case for eutectic growth when crystalline anisotropy is sufficiently weak. The stability of the pattern against long-wavelength perturbations is then governed by the sign of the phase diffusion coefficient  $D_\lambda$  that is function of the periodicity  $\lambda_0$  of the underlying state. To see why, note that any long-wavelength perturbation of the form

$$\lambda(x, t) \approx \lambda_0 [1 + \delta \exp(ikx + \omega_k t)] \quad [5]$$

when substituted into Eq. [2], grows with a rate

$$\omega_k = -D_\lambda k^2 \quad [6]$$

Thus, the array is stable ( $\omega_k < 0$  for all  $k$ ) if  $D_\lambda > 0$ , which implies  $\lambda_0 > \lambda_m$  for eutectic growth, and unstable otherwise. In Eq. [3], we have chosen the symbol  $D_\perp$  to stress the fact that this expression is derived under the normal-growth assumption. It formalizes the Cahn–Jackson–Hunt argument, which predicts a negative (positive) phase-diffusion coefficient for  $\lambda_0 < \lambda_m$  ( $\lambda_0 > \lambda_m$ ).

Equation [6] is valid only for small-amplitude long-wavelength perturbations of the front (*i.e.*, in the limit  $k\lambda_0 \ll 1$ ). Taking into account the parity symmetry of the basic state, the complete stability spectrum can be written as a series in even powers of  $k$ ,

$$\omega_k = \sum_{n=1}^{\infty} A_n k^{2n} \quad [7]$$

with  $A_1 = -D_\lambda$ . An approximate calculation for this spectrum was performed in Reference 10. The result can be written in closed form only in some special cases (for example, symmetric phase diagram and volume fractions), but its generic form can be deduced from the calculation. Here, we are interested in a range of spacings around  $\lambda_m$  where no short-wavelength instabilities occur (that is, instabilities with the same or twice the wavelength of the basic pattern,  $\lambda_0$ <sup>[6,7]</sup>). Even powers of  $k$  other than  $k^2$  are always stabilizing ( $A_n < 0$  for  $n > 1$ ), such that  $\omega_k$  is negative for all  $k$  if  $D_\lambda > 0$ . For  $D_\lambda < 0$ ,  $\omega_k$  first increases as  $k^2$  according to Eq. [6], then passes through a maximum, and becomes negative for  $k$  larger than some marginally stable wave number  $k_c$ . Therefore, this stability spectrum is qualitatively similar to the one of the Cahn–Hilliard equation.<sup>[12]</sup> This allows us to draw an interesting analogy between the lamella elimination instability and spinodal decomposition. For a “homogeneous” initial condition (that is, a constant spacing with small variations), the instability is analogous to bulk spinodal decomposition: a band of wave numbers is unstable, and the fastest modes, corresponding to the maximum of the stability



spectrum, set the characteristic wavelength of the emerging pattern—here, the distance between elimination events. The wall scenario, where the propagation of the instability starts from a heterogeneity, is analogous to surface-directed spinodal decomposition, in which spinodal decomposition is triggered at a surface and propagates into the bulk.<sup>[22]</sup>

### III. EXPERIMENTAL PROCEDURE

#### A. Materials and Setup

The experiments were made with a nearly eutectic  $\text{CBr}_4\text{-C}_2\text{Cl}_6$  alloy prepared with zone refined materials in thin (12- $\mu\text{m}$  thick) glass wall samples (8-mm wide and 60-mm long). The eutectic temperature is 84.4 °C. The constant  $\lambda_m^2 V$  has been measured previously, and is of about  $185 \pm 20 \mu\text{m}^3 \text{s}^{-1}$ .<sup>[23]</sup> The liquid and the solid solutions bounding the eutectic plateau are transparent. The less concentrated solid phase  $\alpha$  is fcc. The more concentrated phase  $\beta$  is bcc. Both phases grow from the melt in a fully nonfaceted way. Therefore, the  $\text{CBr}_4\text{-C}_2\text{Cl}_6$  alloy is an excellent transparent analog of metallic eutectics. The samples are filled by capillarity with a small quantity of the previously prepared alloy under a controlled Argon atmosphere ( $\approx 10$  mbar). They are sealed after a rapid cooling at room temperature. They are then inserted into a directional-solidification device placed under an optical microscope. The temperature gradient is realized between two copper blocks of well-regulated temperatures. The values of  $G$  used ranged from 40 to 110  $\text{Kcm}^{-1}$  ( $\pm 10$  pct). Directional solidification is performed by pulling the sample toward the cold block with a DC motor at a constant velocity  $V$ . We used  $V$  values ranging from 0.125 to 2  $\mu\text{m s}^{-1}$  ( $\pm 4$  pct). Further details can be found in Reference 7, 14, and 23.

We follow the dynamics of the lamellar patterns in real time with an optical microscope coupled to a CCD video camera. The images are stored on tapes with a video recorder, and digitized in a personal computer for further analysis (NIH Image<sup>[24]</sup>). Due to the thinness of the samples, the solid-liquid and solid-solid interfaces appear as mere lines. For the same reason,  $\alpha$ - $\beta$ -liquid triple junction lines are seen as points, thereafter denoted as “trijunction points.” We measure  $\lambda(x)$  from images of lamellar fronts within about  $\pm 0.05 \mu\text{m}$  (Figure 2). The procedure used for extracting the front profile  $\zeta(x)$  was made difficult by the faint contrast of the  $\beta$ -liquid interfaces. Nevertheless, we could obtain a binarized image of the front shape by treating the image numerically, and calculating  $\zeta(x)$ , either by using an automatic fitting procedure, or by averaging  $\zeta(x)$  over each pair of lamellae. By this method, we improved the sensitivity of our measurements, and could detect variations of  $\zeta(x)$  of about 0.1  $\mu\text{m}$ , although the nominal resolution of our optical device is about 1  $\mu\text{m}$ . The dispersion of the experimental  $\zeta(x)$  data when the  $\lambda(x)$  distribution is uniform is  $\pm 0.03 \mu\text{m}$  (Figure 4). We take that value as the error range for  $\zeta$ .

#### B. Selection and Growth of a Eutectic Grain

The standard theory of lamellar eutectic growth does not take capillary anisotropy (*i.e.*, the fact that the surface tension of the solid-liquid and solid-solid interfaces depend on the orientation of these interfaces with respect to the crystal lattices of the two solid phases) into account. However,

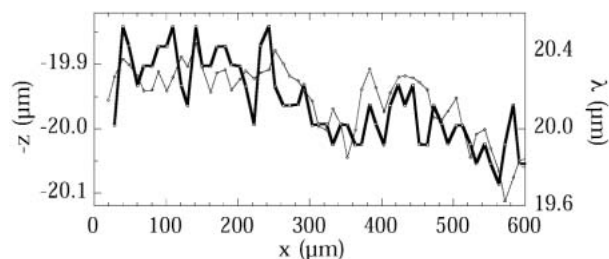


Fig. 4—Lamellar spacing  $\lambda$  (thin line) and average position  $\bar{\zeta}$  of the front (thick line) as a function of  $x$  measured from Fig. 1.

capillary anisotropy, even when it is weak, may perturb lamellar eutectic growth significantly *via* the existence of eutectic grains.<sup>[17]</sup> We recall that a eutectic grain is a region of a lamellar eutectic solid in which all the lamellae of each phase have the same crystal orientation. The main effect of a weak capillary anisotropy is to make the lamellar pattern drift laterally as a whole, *i.e.*, to tilt it with respect to the solidification axis. The “anisotropy driven” tilt angle (which may be as large as 5 deg in  $\text{CBr}_4\text{-C}_2\text{Cl}_6$ ) is different from one eutectic grain to another. When several eutectic grains are present, the lamellae drift in a converging or a diverging way on the two sides of the eutectic grain boundary generating various types of dynamical defects (lamella branching, lamella elimination, tilt, or oscillatory instabilities). To avoid such perturbations, the number of eutectic grain boundaries in the sample must be made as low as possible. This is an essential requirement for fundamental studies in eutectic growth.

For this study, we prepared large, weakly anisotropic (“floating”) eutectic grains following the procedure explained in Reference 2. Since our samples are slightly hypereutectic, the solid in contact with the liquid at rest ( $V = 0$ ) is in the  $\beta$  phase. During the first stages of the solidification, the  $\beta$ -liquid front undergoes a so-called solute redistribution transient. The  $\alpha$  phase emerges onto the front during this transient, and then propagates laterally along the front at a high rate (compared to  $V$ ), masking the pre-existing  $\beta$  grains. This “primary invasion” is followed by a secondary one, during which the  $\beta$  phase re-invades the newly formed  $\alpha$ -liquid front. When the sample is solidified at a very low  $V$  value ( $< 0.1 \mu\text{m s}^{-1}$ ), alternate invasions by the two phases can recur indefinitely, so that, after a while, only one  $\alpha$  and one  $\beta$  crystal remain in contact with the liquid in the central region of the sample. Eventually, an oscillatory instability that occurs during an invasion by the  $\beta$  phase leads to repeated small-scale branching, and hence to a lamellar structure (Figure 5). In this way, a lamellar pattern originating from a single  $\alpha$  crystal and a single  $\beta$  one, thus a single eutectic grain, containing several hundreds of lamellae is created.

#### C. Initial Spacing Distribution

The spacing delivered by the invasion process is a decreasing function of the invasion rate. In general, the latter is so high that the delivered  $\lambda$  value is much smaller than the lower stability limit of the pattern. Therefore, the invasion is followed by numerous lamella elimination events, as can be seen in Figure 5. At the end of the elimination

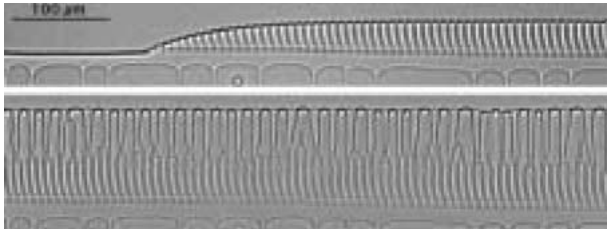


Fig. 5—Top: lamellar branching during a secondary invasion. The initial  $\beta$  polycrystal is still visible in the lower part of the micrograph. A part of the interface between the  $\alpha$  single crystal formed during the primary invasion and the liquid is visible on the left part of the image, ahead of the branching “invasion tongue.” The secondary invasion runs from the right. Bottom: lamella elimination following the invasion process.  $G = 80 \text{ K cm}^{-1}$ ;  $V = 0.5 \text{ } \mu\text{m s}^{-1}$ ;  $C \approx C_E$ .

process, the average value  $\lambda_i$  of the spacing is close to the value of  $\lambda_c$  at the chosen  $V$  (as subsequently discussed). However, because the invasion rate is subject to fluctuations due to the fact that the invaded front is not perfectly planar, the obtained  $\lambda$  distribution is not uniform. It commonly contains  $\lambda$  gradients of an amplitude of  $0.2\lambda_i$  that extend over several tens of  $\lambda_i$ . Since the phase diffusion coefficient is very small for perturbations of large wavelength, those modulations (previously, and somewhat improperly, called “frozen-in” modulations<sup>[7]</sup>) relax extremely slowly. Two methods that we do not describe in details here can be used to avoid, or smooth out, such modulations. One of them consists of making a single eutectic grain grow through a grain selector, *i.e.*, a narrow channel followed by a funnel-shaped region. Another method takes advantage of the “dynamical-selection” mechanism associated with the tilt bifurcation of the pattern.<sup>[25]</sup> Using these methods, we are able to prepare single eutectic grains containing from 100 to 150 pairs of lamellae, in which the width of the  $\lambda$  distribution does not exceed  $\pm 0.04\lambda_i$  (Figure 4).

When a spacing distribution  $\lambda(x)$  has been obtained at a value  $V_1$  ( $2 < V_1 < 3 \text{ } \mu\text{m s}^{-1}$ ) of the pulling velocity, we switch to another value  $V_2$  much smaller than  $V_1$  ( $< 1 \text{ } \mu\text{m s}^{-1}$ ), such that  $\lambda_i < \lambda_c(V_2)$ . Doing this, we exploit the fact that  $\lambda_m$  varies approximately as  $V^{-1/2}$ , so that we effectively vary  $\Lambda = \lambda/\lambda_m$  by performing velocity jumps. We use alloy concentrations close to  $C_E$ , for which the stability range of the pattern is large. Thus, we can perform large changes of  $V$  starting from a relatively large value of  $\Lambda$ , without overpassing the threshold of any of the large- $\Lambda$  short-wavelength instabilities.<sup>[6,7]</sup>

#### IV. EXPERIMENTAL RESULTS

##### A. Direct Measurement of the Undercooling Curve

Using the preceding methods, we created a lamellar pattern with a large-scale spacing modulation  $\lambda(x)$  such that the extreme values of the spacing bracket  $\lambda_m$  (Figure 6). The envelope of that front is shown in Figure 7, together with the corresponding  $\lambda$  profile. We measured the local front undercooling using  $T_{av}(x) = G\zeta(x) + T_0$ , where  $T_{av}$  is the local temperature of the front averaged over one pair of lamellae, and  $T_0$  is an unknown constant. By eliminating  $x$  between  $T_0 - T_{av}(x)$  and  $\lambda(x)$ , we obtain  $T_0 - T_{av}(\lambda)$  data points (Figure 8).<sup>[18]</sup> The thus obtained set of data present a clear

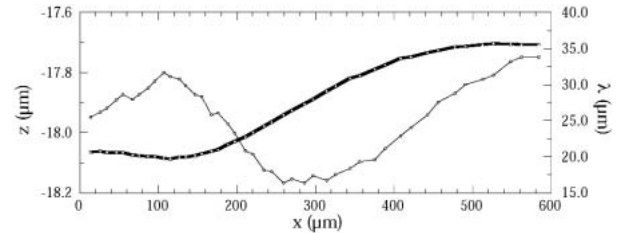
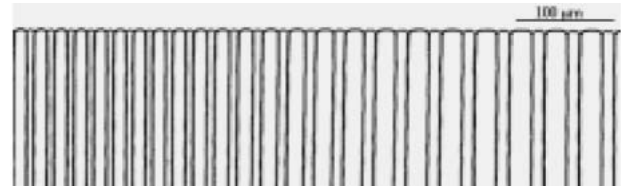
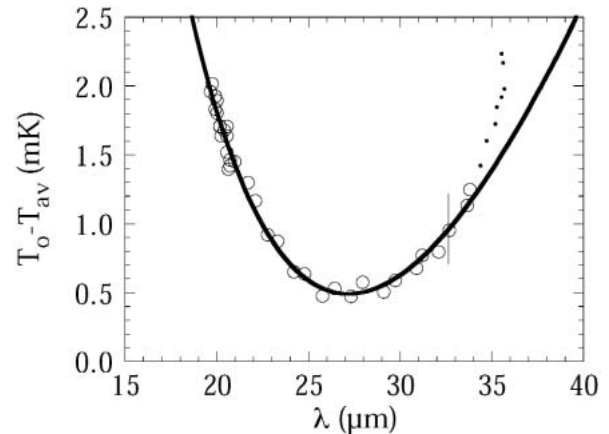


Fig. 7—Shape  $\zeta(x)$  of the envelope of the front (thin line) and distribution  $\lambda(x)$  of the lamellar spacing (thick line) of the micrograph of Fig. 6.



minimum for  $\lambda \approx 27 \text{ } \mu\text{m}$ . We then fit those data to Eq. [1] expressed in the form  $T_0 - T_{av}(\lambda) = \Delta T_m(\lambda/\lambda_m + \lambda_m/\lambda)/2 - \Delta T_0$ , using  $\lambda_m$ ,  $\Delta T_m$ , and  $\Delta T_0 = T_E - T_0$  as adjustable parameters. As shown in Figure 8, the fit is very good for  $\lambda$  smaller than about  $1.25\lambda_m$ . The departure observed beyond this limit is compatible with the one that exists between the numerically calculated curves  $\Delta T(\lambda)$  and the JH approximation.<sup>[5,6]</sup> We performed such measurements for  $V$  ranging from 0.125 to  $0.5 \text{ } \mu\text{m s}^{-1}$ . We found  $\lambda_m^2 V = K_2/K_1 = 193 \pm 16 \text{ } \mu\text{m}^3 \text{ s}^{-1}$  and  $\Delta T_m^2/V = 4K_1K_2 = (2.7 \pm 1.3) \times 10^{-3} \text{ K}^2 \text{ s } \mu\text{m}^{-1}$ . The values calculated from the material constants of  $\text{CBr}_4\text{-C}_2\text{Cl}_6$  given in Reference 23 are  $\lambda_m^2 V = 185 \pm 20 \text{ } \mu\text{m}^3 \text{ s}^{-1}$  and  $\Delta T_m^2/V = (1.2 \pm 0.5) \times 10^{-3} \text{ K}^2 \text{ s } \mu\text{m}^{-1}$ . The agreement is excellent for  $\lambda_m^2 V$ , and reasonable for  $\Delta T_m^2/V$ , given the large error bars.

## B. Lower Stability Limit

A striking feature of the experimental set of  $\Delta T(\lambda)$  data of Figure 8 is that it extends far below  $\lambda_m$ , namely, down to about  $0.7\lambda_m$ . This suggests that the lower stability limit of the pattern is below  $0.7\lambda_m$ . Indeed, we created stationary patterns with a uniform value of  $\lambda$  smaller than  $\lambda_m$ . In order to establish firmly their stability, we studied the temporal evolution of such patterns containing initially small-amplitude, long-range modulations of  $\lambda$ . We measured the phase-diffusion coefficient  $D_\lambda$  as a function of  $\lambda_0$  by studying the relaxation of modulated patterns such as that shown in Figure 9. In that case, the modulation was provoked accidentally by the (almost) simultaneous elimination of two lamellae at a distance of about  $7\lambda_0$  from each other by small glass particles. Such events are generally unwanted for obvious reasons. We used them to study the response of a steady-state pattern (Figure 9 was taken about 30 minutes after the start of the solidification run) to a perturbation without any change of  $V$ , i.e., independently of a solute redistribution transient ( $C_0 \neq C_E$ ), and for  $\lambda_0 \approx \lambda_m$ . Figure 10 shows the  $\lambda$  distribution that corresponds to the case of Figure 9 for successive times. The decay of the dominant modulation mode  $k \approx 2\pi/(7\lambda_0)$  is clearly visible. The inset of Figure 10

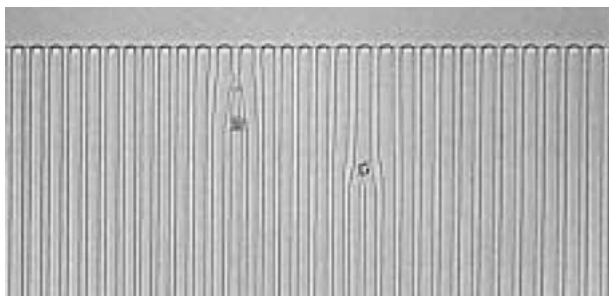


Fig. 9—Lamellar pattern with a large-scale modulation of  $\Lambda_0 \approx 1$ . Dust particles responsible for the elimination of two lamellae are visible in the solid.  $C \approx C_E$ ;  $G = 80 \text{ K cm}^{-1}$ ;  $V = 0.5 \mu\text{m s}^{-1}$ .

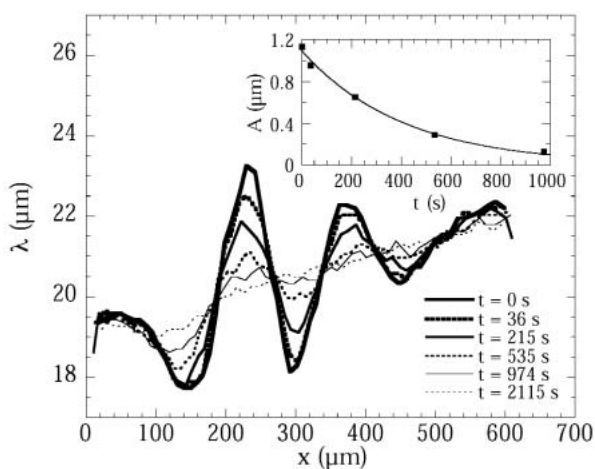


Fig. 10—Experimental measurements of the spacing  $\lambda$  vs  $x$  at different times  $t$  showing the relaxation of a large-scale modulation of a lamellar pattern of  $\Lambda_0 \approx 1$  (same pattern as in Fig. 9). Inset: amplitude  $A$  of the dominant mode (wavelength  $145 \mu\text{m}$ ) vs time, fitted by an exponential law  $A \sim e^{-t/\tau}$  (time constant  $\tau = 410 \text{ s}$ ).

shows its amplitude  $A$  vs time, and the best fit of the data to a decreasing exponential. This behavior is in agreement with Eq. [5], and from the fit, we extract the decay rate  $\omega_k$  and thus the phase-diffusion coefficient  $D_\lambda$ . Here,  $D_\lambda$  is clearly positive, and the array is stable. We found  $D_\lambda = 1.3 \times 10^{-12} \text{ m}^2/\text{s}$ . We repeated the same analysis for a case where  $\lambda_0 \approx 0.88\lambda_m$ . Again, we found a positive phase diffusion coefficient ( $D_\lambda = 7.2 \times 10^{-13} \text{ m}^2/\text{s}$ ). A more detailed analysis of the dependence of the phase diffusion coefficient on  $\Lambda$  and  $G$ , which is based on the phase-field results, is presented subsequently.

From the preceding measurements, we can firmly conclude that  $\lambda_c < \lambda_m$ . We get an estimate of the value of  $\lambda_c$  (for our usual parameter values) by observing the evolution of large, nearly uniform lamellar patterns with  $\lambda_0 < \lambda_m$  over long pulling times. We found that lamella eliminations occur systematically when  $\lambda_0 < 0.7\lambda_m$ , whereas none occurs when  $\lambda_0 > 0.8\lambda_m$ . Thus, we conclude that  $0.7 < \Lambda_c < 0.8$ . The entire set of data of Figure 8 falls within the stable interval, as anticipated.

## C. Lamella Elimination Instability

### 1. Propagation into nearly uniform unstable patterns

We consider first situations in which  $\Lambda_0$  is relatively close to  $\Lambda_c$  ( $\Lambda_0 > 0.6$ ). We shall study in detail two experiments thereafter designated as run 1 (Figure 11) and run 2 (Figures 12 and 13). In both experiments, the initial spacing distribution was first created at relatively high  $V$  ( $> 2 \mu\text{m/s}$ ), and then made unstable ( $\Lambda_0 \approx 0.6$  for run 1, and  $\Lambda_0 \approx 0.66$  for run 2) by a downward velocity jump. Micrographs of Figures 11 and 12 show the large-scale structure of the solid after long-lasting

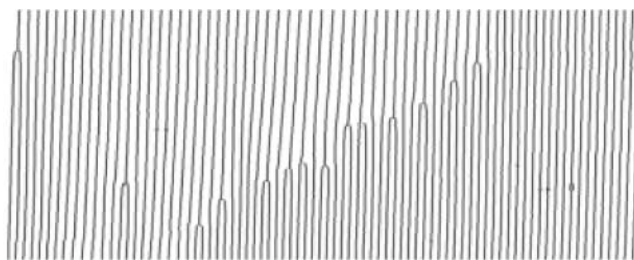


Fig. 11—Low-magnification binarized image of a single eutectic grain (run 1).  $C \approx C_E$ . The bottom line of the image corresponds to a velocity jump from 2 to  $0.75 \mu\text{m s}^{-1}$ . Horizontal dimension:  $985 \mu\text{m}$ . For the sake of clarity, only one  $\alpha$ - $\beta$  interface out of two is shown. The vertical scale is contracted by a factor of 0.3.

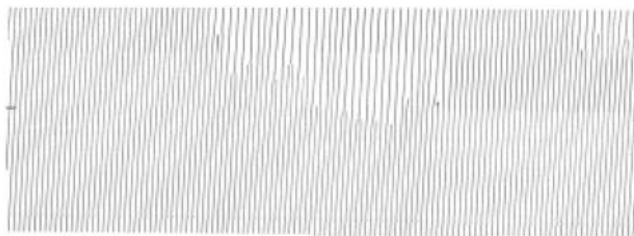


Fig. 12—Single eutectic grain. Same sample as in Fig. 11 (run 2). Response to a velocity jump from  $2.25$  to  $0.5 \mu\text{m s}^{-1}$ . Tick on the left-hand side: time at which the micrograph of Fig. 13 below was taken. Horizontal dimension:  $1580 \mu\text{m}$ . Only one  $\alpha$ - $\beta$  interface out of two is shown. The vertical scale is contracted by a factor of 0.3.



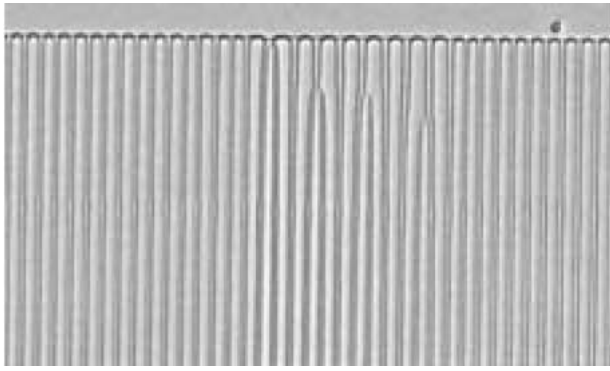


Fig. 13—Propagative lamella elimination instability (run 2; Fig. 12). A dust particle, which is visible in the liquid on the right-hand side of the micrograph, will cause an accidental elimination of a lamella.

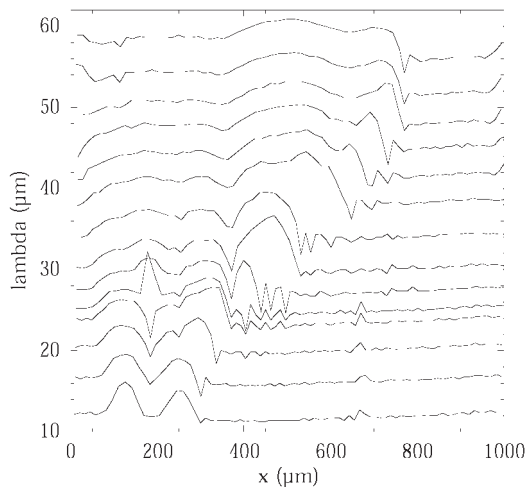


Fig. 14—Spacing distribution  $\lambda(x)$  as a function of time (run 1; Fig. 11). For the sake of clarity, the plots have been shifted along the ordinate axis by an arbitrary quantity proportional to the time interval between two plots. Time lapse between the first and the last plots: 2660 s.

solidification runs. Figure 13 gives an illustration of the shape of the front during the instability process. In such images, the  $\alpha$ - $\beta$  interfaces also represent the trajectories of the trijunction points and provide a natural recording of the spatio-temporal dynamics of the experiment. It can be seen that, during a transient (of about 5 minutes in run 1, and 20 minutes in run 2) after the velocity jump, the pattern remains apparently stationary. Then, a first lamella elimination event occurs, from which the instability propagates into the unstable pattern. The successive eliminations leave behind a lamellar pattern of larger average spacing, which remains stable. We have observed this phenomenon in a large number of other experiments, even when the initial  $\lambda$  distribution was less regular.

Quantitative information on the spatio-temporal dynamics of runs 1 and 2 can be gained by studying the time evolution of the spacing distribution  $\lambda(x)$  (run 1: Figure 14; and run 2: Figures 15 and 16). It clearly appears (*e.g.*, in Figure 16) that the first lamella elimination occurs at, or close to, a minimum of the initial  $\lambda(x)$  distribution, *i.e.*, where the value of  $\lambda_c - \lambda$  is the largest. Moreover, the elimination event itself is preceded by a spatial modulation of the spacing on a very short scale. This is clearly visible in Figure 17, which

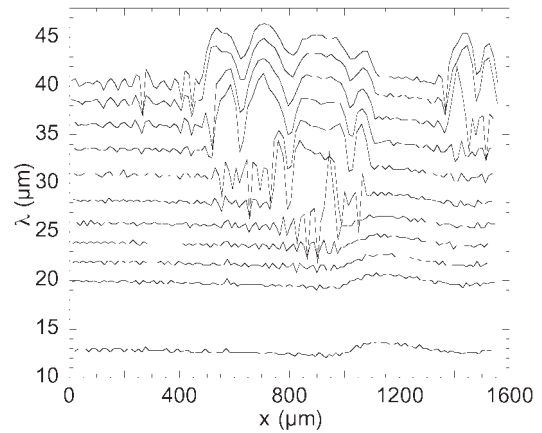


Fig. 15—Spacing distribution  $\lambda(x)$  as a function of time (run 2; Fig. 12). The plots have been shifted along the ordinate axis in the same way as in Fig. 14. Time lapse between the first and the last plots: 2800 s. Note the initiation of the instability at two different positions and times, due to slightly nonhomogeneous initial conditions.

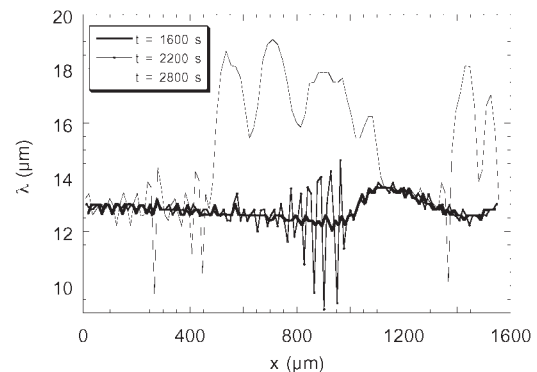


Fig. 16—Spacing distribution  $\lambda(x)$  at three times (run 2), showing the nearly unchanged distribution after a 1600-s pulling time, the first amplification of the spatial oscillation ( $t = 2200$  s), and the distribution at the end of the run ( $t = 2800$  s).

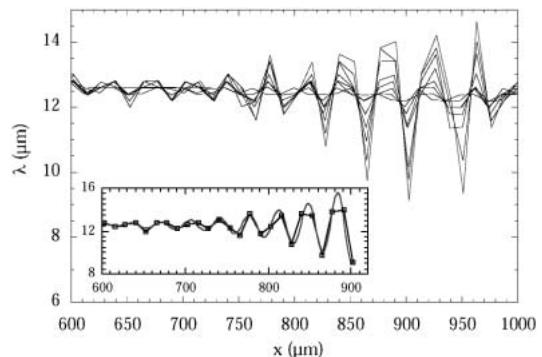


Fig. 17—Evolution of the spacing distribution  $\lambda(x)$  as a function of time in the vicinity of the first lamella elimination event of run 2 (Fig. 12), before the elimination itself takes place. First plot:  $t = 1700$  s. Time interval between two plots: 200 s. Inset: exponentially damped sine with a pseudo period of about  $3.2\lambda_0$  adjusted to the experimental data of the last plot.

represents the time evolution of  $\lambda(x)$  in the region around the first lamella elimination of run 2, just before that event occurs. It can be seen that a modulation of  $\lambda$  of a wavelength

of about  $3.2\lambda_0$  (we measured about  $2.8\lambda_0$  in run 1) develops spontaneously and amplifies until a lamella is eliminated. The modulation remains localized, and appears as a more or less exponentially (spatially) damped patch (inset in Figure 17). The measured amplification time is  $480 \pm 50$  s. The dimensionless amplification rate  $\omega_k\lambda_0/V$  and wave number  $k\lambda_0/2\pi$  (as discussed subsequently) are approximately equal to 0.05 and 0.3, respectively.

Once a lamella has disappeared, this structure survives by propagating into the unstable region of the front. The sequence of lamella eliminations leaves behind a stable pattern ( $\lambda_0 > \lambda_c$ ) with ample spacing modulations that relax in a diffusive way. Thus, at a given time, the entire pattern is made of two regions, the initial unstable one and the new stable one, separated by a wall with a complex internal structure, the essential part of which is a spatially damped short-scale oscillation triggering lamella elimination events at regular time intervals. In the examples presented here, the average height of the  $\lambda$  step within the wall is of about  $5 \mu\text{m}$ . The lateral wall velocity  $V_w$  extracted from the micrographs, is, in units of the pulling speed,  $V_w/V = 0.5 \pm 0.05$  for run 1 and  $0.9 \pm 0.1$  for run 2.

Values of  $\Lambda_0$  very different from  $\Lambda_c$  ( $\Lambda_0 < 0.6$ ) are commonly obtained immediately after a lamellar branching subsequent to a secondary invasion process, as explained previously. In the example of Figures 5 and 18,  $\Lambda_0 \approx 0.4$ , which corresponds to  $\lambda_0 \approx \lambda_c/2$ . The instability develops almost simultaneously everywhere, and leads to the elimination of nearly one lamella out of two. This, and the preceding results, not only suggests that the most dangerous unstable wavelength decreases when the distance  $\Lambda_c - \Lambda_0$  to the threshold increases, but also shows that, depending on the value of  $\Lambda_c - \Lambda_0$ , the lamella elimination instability may be either propagative, or “delocalized” (meaning that it takes place almost simultaneously all over the front).

## 2. Origin of long-lasting modulations

As illustrated in Figure 5, the invasion process used for the formation of large eutectic grains is not perfectly regular, and does not deliver a uniform pattern, but a pattern with modulations of dominant wavelengths ranging from  $100 \mu\text{m}$  to several  $100 \mu\text{m}$  (Figure 18). The relaxation times of the longest of these wavelengths are large compared to the experimental timescale. Indeed, from a typical value of the phase-diffusion coefficient of  $10^{-12} \text{ m}^2/\text{s}$  as measured

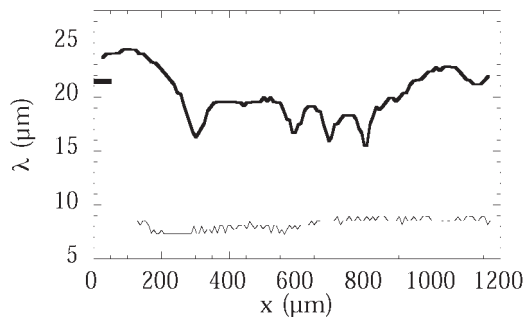


Fig. 18—Spacing distributions  $\lambda(x)$  measured from the same solidification run as in Fig. 5. Thin line: just after the secondary invasion with lamella branching; thick line: after the last lamella elimination event (not shown in Fig. 5).  $\lambda_m \approx 21.2 \mu\text{m}$  (tick on the  $\lambda$ -axis).

previously, we obtain that equilibration on the scale of 1 mm requires times larger than  $10^6$  s. Consequently, the lamellar eutectic pattern remains modulated until the end of the experiment even in the absence of eutectic grain boundaries or other sources of spacing gradients. In Figure 18, the remnant modulation amplitude is typically of order  $\pm 1 \mu\text{m}$ , *i.e.*, less than  $\pm 0.1\lambda_0$ . This is substantially smaller than the width of the spacing distributions measured by Trivedi *et al.* in a series of Pb-based eutectic alloys after long-lasting solidification runs.<sup>[16]</sup> The main reason for this is, most probably, that the samples used by these authors contained numerous eutectic grains, whereas ours were single eutectic grains. Finally, it is interesting to note in Figure 18 that the final value of  $\lambda_0$  ( $19.7 \mu\text{m}$ ) is smaller than  $\lambda_m$ .

## V. NUMERICAL SIMULATIONS

### A. Phase-Field Model

We simulate eutectic solidification of a generic A-B alloy with a phase-field model similar to previous works.<sup>[26,27,28]</sup> An order parameter  $\phi$ , which distinguishes between solid ( $\phi = +1$ ) and liquid ( $\phi = -1$ ), is coupled to the dimensionless concentration field,

$$u \equiv \frac{C - C_E}{(C_\beta - C_\alpha)/2} \quad [8]$$

where  $C$  is the mole fraction of B, and  $C_\alpha$ ,  $C_\beta$ , and  $C_E$  are the concentrations of the two solids and the liquid at the eutectic temperature  $T_E$ . We note that the phase field is a non-conserved variable, whereas the concentration must satisfy a local conservation law. The dynamics for  $\phi$  and  $u$ ,

$$\tau \partial_t \phi = - \frac{\delta F}{\delta \phi} \quad [9]$$

$$\partial_t u = \nabla \cdot \left( M(\phi) \nabla \frac{\delta F}{\delta u} \right) \quad [10]$$

where  $\tau$  is a relaxation time and  $M$  a mobility, are derived from the free energy functional

$$F = \int_V dV \left[ \frac{W_u^2}{2} |\nabla u|^2 + \frac{W_\phi^2}{2} |\nabla \phi|^2 + f(\phi, u, T) \right] \quad [11]$$

where  $V$  is the volume of the system and

$$f(\phi, u, T) = f_{DW}(\phi) + \frac{1 + h(\phi)}{2} f_s + \frac{1 - h(\phi)}{2} f_l \quad [12]$$

is the bulk free-energy density. It is the sum of the standard double-well

$$f_{DW} = -\phi^2/2 + \phi^4/4 \quad [13]$$

and a concentration-dependent part that interpolates between the bulk free energy of liquid and solid,

$$f_l = u^2/2 \quad [14]$$

$$f_s = (1 - u^2)^2/8 - \alpha(T_E - T)/T_E \quad [15]$$

with  $\alpha$  being a dimensionless latent heat and  $h(\phi) = 3(\phi - \phi^3/3)/2$ . This bulk free-energy density has three local minima that correspond to the two solids ( $\phi = 1$ , and  $u = \pm 1$ )



and the liquid ( $\phi = -1$ , and  $u = 0$ ). The bulk values are connected by diffuse interfaces of width  $\sim W_u$  and  $W_c$ . In the following, we will assume  $W_u = W_c = W$ . Furthermore, we use the mobility

$$M(\phi) = D \left[ 1 - \frac{(1 + \phi)^4}{16} \right] \quad [16]$$

where  $D$  is the solute diffusivity in the liquid. This expression makes the diffusivity in the solid vanish and yields efficient computations.<sup>[28]</sup> Directional solidification is implemented in the standard frozen temperature approximation, which assumes that the temperature field is fixed by the experimental setup

$$T(z, t) = T_E + G(z - Vt) \quad [17]$$

The preceding free-energy functional yields a phase diagram that is completely symmetric with respect to the interchange of A and B, and that has parallel liquidus and solidus lines for each two-phase equilibrium for temperatures close to  $T_E$ . More general models can easily be constructed, but our purpose here is to study some general aspects of the lamella elimination process rather than to model precisely a specific substance.

The properties of the model have been discussed in detail in Reference 28, and we will give here only a brief summary of the results. The characteristic length scales involved in directional solidification are the diffusion length  $l_D = D/V$ ; the two thermal lengths  $l_T^\nu = |m_\nu| \Delta C / G$ ,  $\nu = \alpha, \beta$ , where  $m_\nu$  are the liquidus slopes in the phase diagram and  $\Delta C = C_\beta - C_\alpha$ ; and the capillary lengths  $d_0^\nu = \Gamma_\nu / (m_\nu \Delta C)$ , where  $\Gamma_\nu = \gamma_{\nu L} T_E / L$  are the Gibbs–Thomson constants, with  $\gamma_{\nu L}$  being the  $\nu$ -liquid surface tension and  $L$  the latent heat. In our model, with a symmetric phase diagram,  $l_T^\alpha = l_T^\beta = l_T$  and  $d_0^\alpha = d_0^\beta = d_0$ . Since our free-energy density is dimensionless, surface tension has a dimension of length, and numerically, we find  $\gamma_{\nu L} = 1.04 W$ . Setting  $T_E = \alpha = 1$ , we find  $m \Delta C = m_u \Delta u = 2$ ,  $d_0 = 0.52 W$ ,  $l_D = D/V$ , and  $l_T = 2/G$ . In the following, we will measure lengths, times, and temperature in units of  $W$ ,  $\tau$ , and  $T_E$ , respectively, unless stated otherwise.

The phase-field equations were discretized on a regular square grid of spacing  $\Delta x = W$  using standard finite-difference formulas, and integrated in time by an Euler scheme with time-step  $\Delta t = 0.025 \tau$ . We used  $D = 1$ ,  $V = 0.01 W/\tau$ , and various values for  $G$ . Periodic boundary conditions were used in the direction parallel to the isotherms (normal to the growth direction). Far ahead of the interface, the concentration  $u$  was fixed, usually to the eutectic composition  $u = 0$ ; behind the interface, the diffusivity falls to zero and no evolution occurs. Therefore, no boundary condition needs to be specified on the solid side. When the interface has grown by one lattice spacing, the entire simulation box is shifted backward.

### B. Stability Limit

We first performed small simulations of individual lamella pairs to establish the undercooling vs spacing relation. The simulations in boxes of width  $\lambda/W$  and length 1000 were started with an initial condition of two flat lamellae in contact with the liquid at the eutectic composition. On a time

scale of a few  $\lambda^2/D$ , the interface relaxes to a steady state. The undercooling was determined by

$$\Delta T(t) = -G \left( \frac{1}{\lambda} \int_0^\lambda \xi(x, t) dx - Vt \right) \quad [18]$$

where the  $z$  position of the interface,  $\xi(x)$ , defined as the position of the zero crossing of the phase field, is obtained by interpolating  $\phi$  along  $z$  at fixed  $x$ . The result for the undercooling as a function of  $\lambda$  for two different temperature gradients is shown in Figure 19. In agreement with the JH theory, the undercooling is almost independent of  $G$ . The minimum undercooling spacing is  $\lambda_m \approx 33.3 W$ .

Next, we performed simulations of large-scale arrays. To this end, the converged steady-state solution of the small runs was stored, replicated  $N$  times, and used as an initial condition. In order to test the stability of the array, this perfectly periodic state was perturbed at  $t = 0$  by shifting the interface along  $z$  by a different random amount of order  $W$  for each value of  $x$ ; the new values for both fields on the grid points were obtained by linear interpolation. For stable arrays, the perturbation decays and we return to the perfectly periodic state. For unstable arrays, the short-wavelength part of the noise is rapidly smoothed out, but the long-wavelength components trigger the lamella elimination instability, which develops on a slow timescale.

To obtain quantitative information about array stability, we monitor in detail the trijunction points. The positions ( $x_n^\nu, z_n^\nu$ ) of the trijunction to the right of the  $n$ th  $\nu$ -lamella are obtained by searching the intersections of the  $\phi = 0$  and  $u = 0$  level sets. Their steady-state values ( $\bar{x}_n^\nu, \bar{z}_n^\nu$ ) are known, and we define the trijunction displacements

$$\xi_n^\nu = z_n^\nu - \bar{z}_n^\nu \quad [19]$$

$$y_n^\nu = x_n^\nu - \bar{x}_n^\nu \quad [20]$$

as well as their discrete Fourier transforms,

$$X_\nu(\kappa, t) = \frac{1}{N} \sum_{n=0}^{N-1} \xi_n^\nu \exp(2\pi i \kappa n) \quad [21]$$

$$Y_\nu(\kappa, t) = \frac{1}{N} \sum_{n=0}^{N-1} y_n^\nu \exp(2\pi i \kappa n) \quad [22]$$

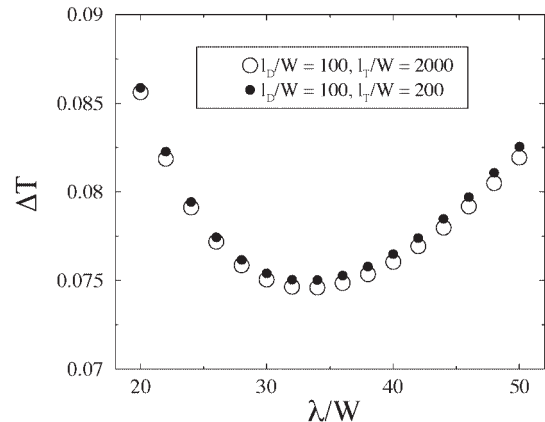


Fig. 19—Undercooling vs spacing obtained from phase-field simulations.

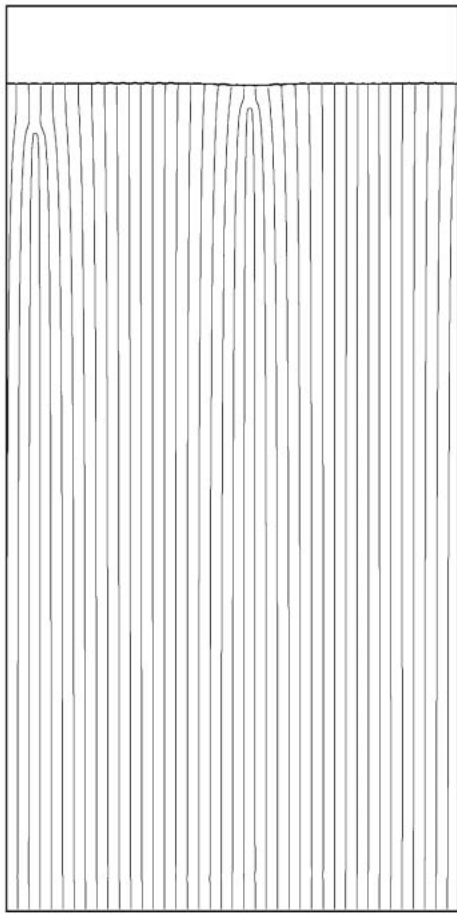


Fig. 20—Phase-field simulation of an unstable array for  $\lambda_0/W = 28$  ( $\Lambda_0 = 0.84$ ),  $l_D/W = 100$ , and  $l_T/W = 2000$ . Growth direction is from bottom to top.

where  $\kappa = k\lambda_0/(2\pi)$  is a dimensionless wave number, and  $\lambda_0$  is the spacing of the underlying steady-state solution.

An example for the evolution of an unstable array is shown in Figure 20, for  $\lambda_0/W = 28$  ( $\Lambda_0 = 0.84$ ) and 20 lamellae pairs. The modulus of the corresponding Fourier amplitudes,  $|Y_\alpha(\kappa, t)|$  is plotted in Figure 21 for the long-wavelength modes. Three stages can be distinguished: at the beginning of the run, the amplitudes evolve rapidly due to the relaxation of the short-wavelength components of the noise; then, they grow exponentially, as expected from Eq. [5]. Finally, they deviate from exponential behavior due to the fact that lamella elimination events are approached; the Fourier amplitudes are not plotted after the eliminations because the number of triple points (and, hence, the wave number  $\kappa$ ) has changed.

In the intermediate regime, the growth rate  $\omega_k$  of the eigenmodes can be obtained by a fit to the expression  $|Y_\alpha(\kappa, t)| \sim \exp(\omega_k t)$ , and the complete stability spectrum can be extracted from a single run. Two examples are shown in Figure 22, one for the run of Figure 20 and the other for the same initial spacing and pulling speed, but a 10 times higher temperature gradient. It can be seen that the second run is stable, although  $\Lambda_0 = 0.84$  is significantly lower than 1. To obtain the phase-diffusion coefficient, following Eq. [7], we fitted the stability spectra with a third-order polynomial in  $\kappa^2$  and extracted the coefficient of the  $\kappa^2$  term. Plots of

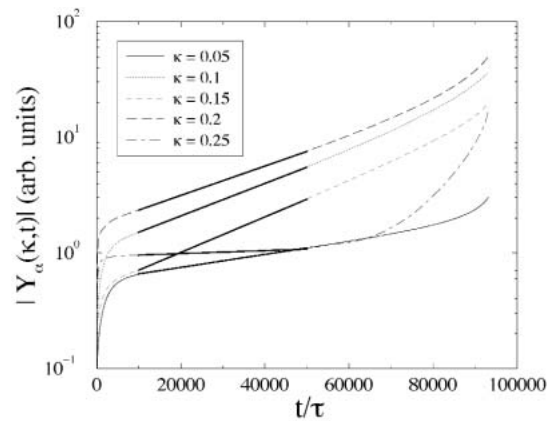


Fig. 21—Fourier amplitudes of lateral trijunction displacements vs time for different dimensionless wave vectors  $\kappa = k\lambda_0/(2\pi)$ . The thick line segments are fits to exponential functions, which are used to extract the growth rates.

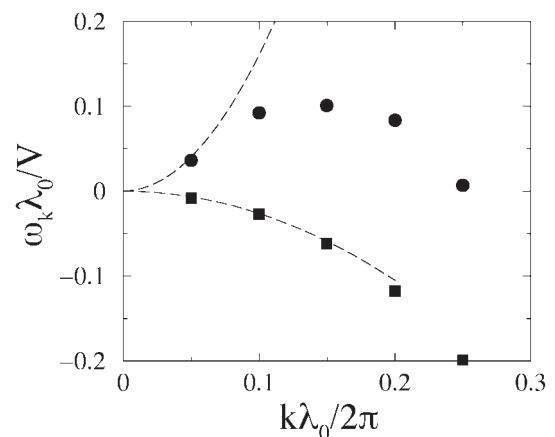


Fig. 22—Stability spectra for the array shown above (circles) and another stable one obtained with a 10 times higher temperature gradient ( $l_T/W = 200$  squares). Dashed lines: refer to text.

Eq. [6] with the extracted  $D_\lambda$  are shown as dashed lines in Figure 22. For the unstable arrays, a  $\sim 10$  pct error bar must be accepted due to the fact that the higher order terms become important for quite small  $\kappa$ .

We note that at the end of the run shown in Figure 20, two lamellae are eliminated, which corresponds to a wave number of  $\kappa = 0.1$ , whereas the maximum of the stability spectrum is at  $\kappa \approx 0.15$ . However, this is not in contradiction with the idea that the characteristic wavelength of the pattern should be set by the mode with maximum growth rate. In our simulations, we start from a random initial condition, and for each realization, the different modes start with different initial amplitudes. This can be clearly seen in Figure 21. Hence, the dominant mode should be determined by averaging either over a larger system or numerous runs, both of which require considerable computational effort.

### C. Lamella-Elimination Instability

To simulate a propagating wall, we changed the boundary conditions on the sides of the box to no-flux, which corresponds to a closed system. The box was filled with thin lamellae that constitute an unstable array. One single larger

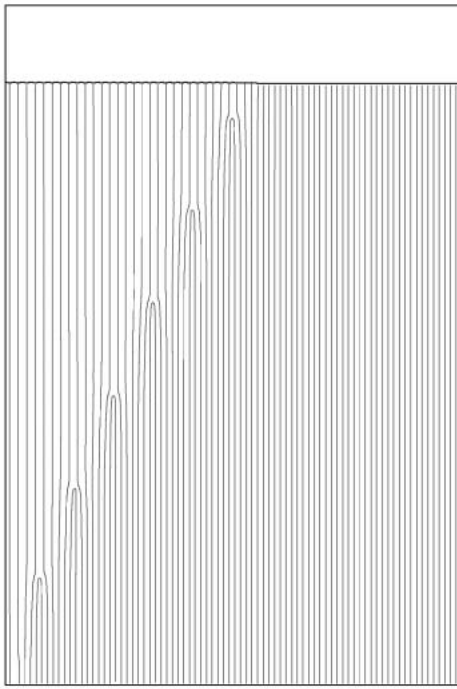
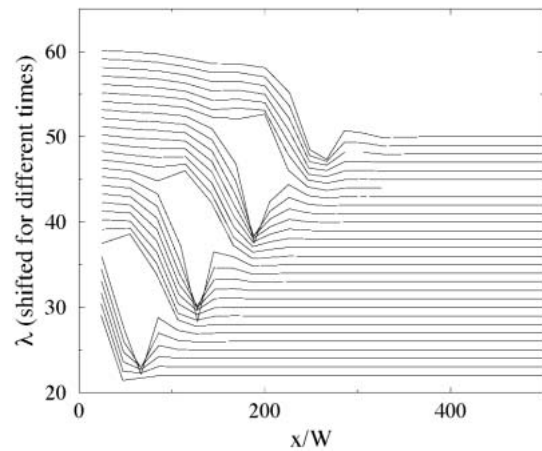


Fig. 23—Propagating instability. One larger lamella was initially placed at the left side of the simulation box. No-flux boundary conditions are applied on both sides. Initial lamellar spacing:  $\lambda_0/W = 20$ ;  $V = 0.01$ ;  $G = 0.007$ .

**Table I. Characteristics of Simulated Propagating Walls**

Pulling velocity $V$	0.01	0.01	0.01	0.01
Temperature gradient $G$	0.007	0.007	0.004	0.001
Initial spacing $\lambda_0$	20	24	24	24
$V_w/V$	0.44	0.13	0.27	0.53
$\lambda_e/\lambda_0$	3.5	5.3	4.7	5.3
Final spacing $\lambda_f$	28.0	29.3	30.5	unstable

lamella was placed at one border, and no other perturbation was applied. The resulting evolution is shown in Figure 23. The larger lamella grows slightly ahead of the thinner ones, which leads to a “squeezing” of the neighboring thinner lamellae, and ultimately to the elimination of one lamella. As a result, larger lamellae are created close to the single initial one. This process repeats itself, and a regularly spaced series of lamella eliminations takes place. It can be seen that this advance of the larger lamella has a perfectly well-defined velocity. This velocity depends on the lamellar spacing ahead of the front and on the applied temperature gradient. In Table I, we list the lateral wall velocity  $V_w$ , the lateral distance between elimination events  $\lambda_e$ , and the final spacing behind the wall  $\lambda_f$  for different runs (we recall that  $\lambda_m = 33.3$ ); the first column corresponds to the run shown in Figure 20. The evolution of the spacings with time for the run of Figure 23 is shown in Figure 24. Note the similarities to Figure 14. As in the experiment, there exists an oscillatory “precursor” structure in the  $\lambda$  curves that propagates into the unstable front. However, in the simulation, it is damped much more rapidly than in the experiments, such that only one oscillation can be clearly identified. This discrepancy is most likely due to the widely different control parameters of simulation and experiments. In particular, because different regions



of the fronts are coupled diffusively, we expect the length of this precursor structure to depend on the Peclet number  $Pe = \lambda_0 l_D = \lambda_0 V/D$ , which is of about 0.2 in the simulations, but one order of magnitude smaller in the experiments.

## VI. DISCUSSION

### A. Stability Limit

Our data, both from experiments and simulations, clearly demonstrate that lamellar arrays can be stable for spacings that are substantially smaller than  $\lambda_m$ . Therefore, the prediction for the phase diffusion coefficient of Eq. [3] is not valid. Let us now examine what part of the derivation of this equation has to be revised.

The experimental data shown in Figure 10 and the numerical results of Figure 21 prove that the dynamics of the lamellar array can indeed be described as a linear superposition of eigenmodes of the form given by Eq. [5]. Furthermore, from Figure 22, we conclude that the long-wavelength part of the stability spectrum is  $\sim k^2$ , such that the phase-diffusion equation applies. Yet, the phase-diffusion coefficient extracted from both simulations and experiments does not agree with the prediction of Eq. [3]. Because the spacing-undercooling temperature relation is not appreciably modified by the large-scale inhomogeneities, the only remaining questionable hypothesis is Cahn’s rule of normal growth.

Indeed, a detailed analysis of the trijunction motion<sup>[28]</sup> shows that there is a small violation of Cahn’s normal-growth assumption. Namely, trijunctions move also *parallel* to the envelope of the composite front with a velocity that is proportional to the local gradient of the spacing, in addition to their normal motion. This effect is small in the sense that the resulting tilt of the lamellae with respect to the front envelope is less than 1 deg for typical conditions.<sup>[28]</sup> It is therefore impossible to extract it directly from experimental measurements. However, this small effect has a measurable impact on the phase-diffusion coefficient. The motion of the trijunctions can be expressed as  $\partial_t y(x, t) = -V \partial_x \xi(x, t) + D_{\parallel} \partial_x \lambda(x, t)/\lambda_0$ , where  $D_{\parallel}$  is an unknown constant with the dimension of a diffusion coefficient. Indeed, repeating Langer’s analysis with the preceding



relation instead of the normal-growth conjecture, we obtain again the phase-diffusion equation, but now with

$$D_{\lambda} = D_{\perp} + D_{\parallel} \quad [23]$$

Therefore, values for  $D_{\parallel}$  can be extracted from our experimental and simulation data by subtracting the theoretical expression for  $D_{\perp}$  from the measured values of  $D_{\lambda}$ . The results are plotted in Figure 25. The dimensionless ratio  $D_{\parallel}/(V\lambda_0)$  varies with  $\Lambda_0$ , but is almost independent of  $G$  and  $V$ . We find that the simple form

$$D_{\parallel}/(V\lambda_0) \approx A\Lambda_0 \quad [24]$$

with  $A \approx 0.15$  gives a reasonable fit to our phase-field simulation results, as shown in Figure 25. Remarkably, the values of  $D_{\parallel}$  extracted from the experiments are reasonably close to the same curve, even though the two alloy systems are different and we use widely different control parameters.

From the empiric Eq. [24], a prediction for the critical spacing for the onset of instability  $\Lambda_c = \lambda_c/\lambda_m$  can be obtained by setting  $D = D_{\perp} + D_{\parallel} = 0$ , which, using the JH expression for  $\lambda_m$  and Eqs. [3] and [24], yields the cubic equation

$$1 - \frac{1}{\Lambda_c^2} + \frac{AG}{K_1 V} \Lambda_c = 0 \quad [25]$$

Clearly,  $\Lambda_c$  depends on the ratio  $G/V$ . In Figure 26, we plot the values of  $\lambda_m$  and  $\lambda_c$  obtained for  $\text{CBr}_4\text{-C}_2\text{Cl}_6$  using  $K_1 = 1.9 \times 10^{-3} \text{ K s } \mu\text{m}^{-2}$ ,  $A = 0.15$ , and  $G = 48 \text{ K/cm}$  vs  $V$ . The lowest spacing observed in the experiment of Figure 8 is marked by a cross and turns out to be just above the predicted stability threshold.

It is worthwhile to compare the above prediction to previous experimental observations in metallic systems. For this purpose, we have reproduced the experimental data of Trivedi *et al.*,<sup>[16]</sup> and plotted the curve calculated from Eq. [25] for the Pb-62wt pct Sn alloy in Figure 27. In the calculation, we set  $A = 0.15$  and took the values of  $K_1$  and  $K_2$  calculated from independent measurements of the physical constants of the alloy.<sup>[16,29]</sup> No adjustable parameter comes into play. The agreement between the experimental values of the lowest measured value of  $\lambda$  and the calculated values of  $\lambda_c$  is remarkably good. However, the deviation of  $\lambda_c$  from the law  $\lambda \propto V^{-0.5}$  at the lowest explored value of  $V/G$  is only  $\approx 6$  pct in this alloy. This deviation is much smaller than in the organic system studied here ( $\approx 30$  pct), and probably comparable to the experimental uncertainty. This uncertainty is also enhanced by the lack of direct measurement of  $\lambda_m$  in the metallic system, which prevents us from testing the accuracy of the calculations of  $K_1$  and  $K_2$ . Therefore, experiments in this system for  $V/G$  values about one order of magnitude smaller than shown in Figure 27 would be needed to provide a more substantive test of the prediction of Eq. [25].

Two previous theoretical analyses have predicted that  $\lambda_c$  should be smaller than  $\lambda_m$ . The one by Brattkus *et al.*,<sup>[12]</sup> however, is valid only in the limit where  $G$  is large (more precisely,  $l_T \ll l_D$ ). In this limit, the lamellae are flat except in the immediate vicinity of the trijunction points where the curvature is fixed by the equilibrium between capillarity and the temperature gradient. This analysis is not

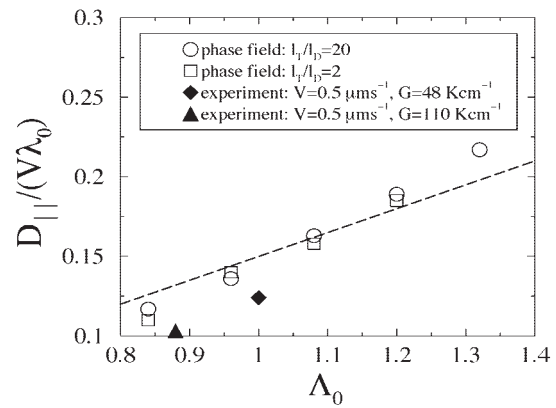
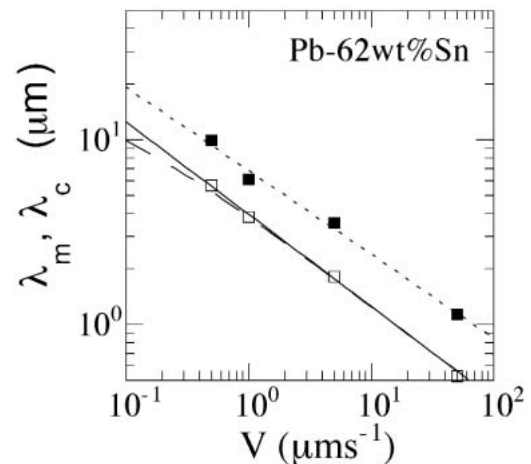
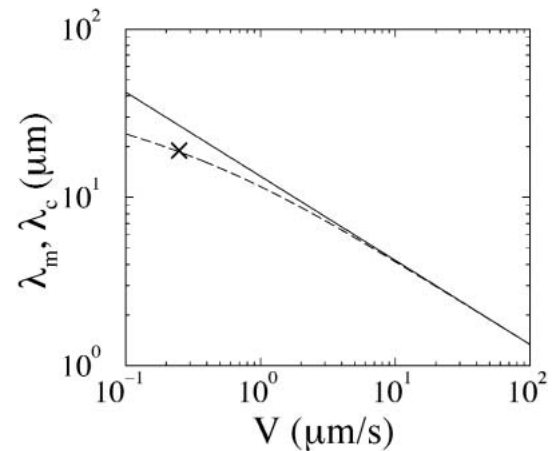


Fig. 25—Phase diffusion coefficient  $D_{\parallel}$  associated with lateral trijunction motion, as extracted from phase-field simulations and experiments.



applicable for the  $G$  values of our simulations and experiments ( $l_T > l_D$ ); here, the lamellae are gently curved over their entire width. The analysis by Chen and Davis<sup>[13]</sup> is valid for any value of  $G$ , but predicts a departure of  $\lambda_c$  from  $\lambda_m$  that is about one order of magnitude smaller than found here and predicted by Eq. [25]. It therefore does not seem to capture the lateral trijunction motion. The most likely reason is that this analysis is based on a multiscale expansion, which neglects, to lowest order, the influence of the local geometry on the diffusion field. We believe that the lateral motion of the trijunctions is due to a coupling between the diffusion field and the nonplanar front geometry on the scale of the individual lamellae; such effects would appear only at higher orders in the calculations cited previously.

### B. Lamella Elimination Instability and Spacing Selection

We have identified two different scenarios for the dynamics of the instability. Lamella elimination can either take place almost simultaneously over large parts of the front, or start from a localized perturbation and propagate along the front. This is analogous to bulk- and surface-directed spinodal decomposition, respectively. For the Cahn–Hilliard equation, the wall propagation velocity and the periodicity of the resulting stable pattern are quantitatively well predicted by the marginal stability theory,<sup>[19]</sup> which uses only the stability spectrum of the unstable state as an input. We have tried to apply this theory to obtain a prediction for the wall velocity of the lamella elimination instability. While it yields a good order of magnitude estimate, the exact values obtained depend on the order of the fit used for the dispersion relation (that is, the number of coefficient  $A_{2n}$  of Eq. [7] that are retained). Therefore, no quantitative prediction for this velocity can be given at the present stage.

In both scenarios, the fraction of lamellae that is eliminated depends on the distance of the initial array from the stability threshold. The propagative process leads to a stable state when  $\lambda_c - \lambda_0$  is sufficiently small, and to an unstable state (followed by a second wave of eliminations), when  $\lambda_c - \lambda_0$  is large (simulations not shown). The delocalized process always leads to an unstable state. In a large sample, different scenarios can occur simultaneously in different parts of the sample. Therefore, the “pathway” followed by the instability largely depends on the initial configuration and the size of the system. As a consequence, the final spacing also depends on the initial configuration and the system size. Hence, there is no dynamic selection of the spacing in the strict sense.

Remarkably, the final spacings are always very close to the stability threshold. In the absence of an analytical expression for the stability spectrum, no precise general argument can be given that explains this “weak” selection. Qualitatively, the argument is as follows. Both for the delocalized and for the propagative scenario, the selected wave number  $\kappa$  decreases with the distance to the stability threshold. Since the fraction of lamellae that is eliminated is equal to  $\kappa$ , the change in  $\Lambda$  is equal to  $1/(1 - \kappa)$ . Therefore, when the system starts close to the threshold, the spacing change will be small, and hence the final stable state will remain close above the threshold.

The inhomogeneities which remain after the eliminations are subsequently smoothed out by phase diffusion. Since the phase-diffusion coefficient vanishes at the stability threshold, this process is generally very slow. As a consequence, even in the absence of grain boundaries or other perturbations, the pattern always retains some degree of heterogeneity over experimentally accessible time scales.

## VII. CONCLUSIONS AND FUTURE PROSPECTS

In summary, we have established both experimentally and theoretically that the lower stability bound of lamellar eutectic patterns does not coincide with the minimum-undercooling spacing, as was previously assumed, but can be significantly smaller than  $\lambda_m$ , at least for two-dimensional systems. Experimentally, our ability to measure for the first time directly the undercooling-spacing relation, and hence  $\lambda_m$ , played a key role in reaching this conclusion.

We have shown that this overstability below the minimum undercooling spacing originates from the motion of trijunctions parallel to the envelope of the solidification front that opposes the formation of gradients of spacing along the front. Because of this lateral motion, solid-solid interfaces do not grow exactly normal to this envelope. The angular deviation from the normal, which is of the order of 1 deg, is too small to be detectable experimentally, but nonetheless has a strong effect on the stability that is, itself, precisely measurable.

The range of overstability,  $\lambda_m - \lambda_c(V)$ , increases as the ratio  $V/G$  decreases. We have modified Langer’s derivation of the phase-diffusion equation to take into account the lateral motion of trijunctions, and thereby obtained a new prediction for the lower bound of stability  $\lambda_c(V)$  as a function of  $V/G$ . To do so, we have phenomenologically assumed that the lateral velocity of trijunctions is proportional to the local gradient of spacing along the front, and extracted from the phase-field simulations how the proportionality constant in this relation depends on various parameters. We have found that the ratio of this constant and the initial spacing ( $D_{||}/\lambda_0$ ) is to a good approximation proportional to the product of the growth rate  $V$  and the ratio  $\Lambda_0$  of the initial spacing to the minimum-undercooling spacing in a way that is remarkably identical in the experiments and the simulations despite the different alloy systems used. A rigorous derivation of this phenomenological law from the basic governing sharp-interface equations of eutectic growth is an interesting future prospect, but appears highly nontrivial at this point.

From a more general standpoint, overstability implies that coupled growth can be stable even if the undercooling-spacing relation has a negative slope. For peritectic alloys, Boettinger<sup>[30]</sup> has shown theoretically that the undercooling-spacing relation does not have a minimum and exhibits negative slopes, such that peritectic coupled growth should be unstable according to the Cahn–Jackson–Hunt line of argument. Yet, Vandyoussefi *et al.* have recently observed stable coupled growth in the concerned concentration range of the Fe–Ni peritectic system.<sup>[31]</sup> The overstability of lamellar growth due to the lateral motion of the trijunctions demonstrated in the present article may reconcile Vandyoussefi *et al.*’s observations and theory.

Our results reinforce the view that the selection of the lamellar spacing is not unique even within a single spatially extended eutectic grain. Furthermore, they shed new light on the origin of this nonuniqueness. We find that the selection is strongly history dependent in a way that is strikingly similar to spinodal decomposition. Depending on the initial condition, the selection can be propagative, with an initially localized spatial domain of stable spacing ( $\lambda > \lambda_c$ ) invading nearby domains of unstable spacing ( $\lambda < \lambda_c$ ), or spatially delocalized if all spacings along the front are initially unstable. Both scenarios are likely to occur simultaneously in multigrain samples. Even though these mechanisms do not select a unique spacing, they select a relatively narrow range of spacings slightly above  $\lambda_c$ . This weak selection close to  $\lambda_c$  is simply a consequence of the fact that the eutectic spacing generally coarsens in time starting from a fine initial structure, and this coarsening process stops once stability is achieved everywhere along the front.

In this study, we have focused our attention on the small spacing stability limit of eutectic growth. The range of spacing that survives over experimental time scales could, in principle, also be influenced by the largest stable spacing. Previous numerical<sup>[6]</sup> and experimental studies<sup>[7]</sup> of TDS have shown that this spacing is about twice  $\lambda_m$  at the eutectic composition, where the range of stable spacing is largest, with the exact value being dependent on the phase diagram.<sup>[6]</sup> In contrast, the highest measured spacings in the fully three-dimensional experiments of Trivedi *et al.*<sup>[16]</sup> are typically only 40 to 50 pct larger than  $\lambda_m$ , as shown in Figure 27. This is so even though these experiments are carried out in multigrain samples, where the lamellar-spacing distribution is usually larger than in monograin samples.

One possible reason for this difference is that the upper limit of stability of eutectic growth may be smaller in three than two dimensions. This seems likely because other modes of instability are allowed in three dimensions that are not allowed in two (such as the classical zig-zag instability of convection rolls<sup>[11]</sup>), and such modes can further restrict the range of stable spacings. Another possibility is the aforementioned history-dependent weak selection that tends to select spacings slightly larger than the smallest stable spacing, independently of the stability limit at large spacing. Further exploration of these possibilities is needed to understand the deviation of the average spacing below the  $\propto V^{-1/2}$  law at small  $V$ ,<sup>[5,15]</sup> which remains an unsolved puzzle. If weak selection still prevails in bulk samples, and the small spacing stability limit is the same in two and three dimensions, then the overstability below the minimum undercooling elucidated here may be the reason for this deviation. In contrast, if the average spacing is determined by the entire range of stable spacings, the answer may lie in the velocity dependence of the upper stability limit. Experiments and simulations are presently underway to explore these scenarios.

## ACKNOWLEDGMENTS

This work was supported by the Centre National d'Etudes Spatiales, France, and by the United States Department of Energy under Grant No. DE-FG02-92ER45471.

## REFERENCES

1. W.J. Boettinger, S.R. Coriell, A.L. Greer, A. Karma, W. Kurz, M. Rappaz, and R. Trivedi: *Acta Mater.*, 2000, vol. 48, pp. 43-70.
2. S. Akamatsu, S. Moulinet, and G. Faivre: *Metall. Mater. Trans. A*, 2001, vol. 32A, pp. 2039-48.
3. H. Nguyen Thi, Y. Dabo, B. Billia, D. Camel, and B. Drevet: *J. Phys. IV (France)*, 2001, vol. 11, pp. 161-67.
4. K.A. Jackson and J.D. Hunt: *Trans. TMS-AIME*, 1966, vol. 236, pp. 1129-42.
5. K. Kassner and C. Misbah: *Phys. Rev. A*, 1991, vol. 44, pp. 6513-22.
6. A. Karma and A. Sarkissian: *Metall. Mater. Trans. A*, 1996, vol. 27, pp. 635-56; A. Sarkissian: Ph.D. Thesis, Northeastern University, Boston, MA, 1996.
7. M. Ginibre, S. Akamatsu, and G. Faivre: *Phys. Rev. E*, 1997, vol. 56, pp. 780-96.
8. V. Seetharaman and R. Trivedi: *Metall. Trans. A*, 1988, vol. 19A, pp. 2955-64.
9. J.S. Langer: *Phys. Rev. Lett.*, 1980, vol. 44, pp. 1023-26.
10. V. Datye and J.S. Langer: *Phys. Rev. B*, 1981, vol. 24, pp. 4155-69.
11. M.C. Cross and P.C. Hohenberg: *Rev. Mod. Phys.*, 1993, vol. 65, pp. 851-1112.
12. K. Brattkus, B. Caroli, C. Caroli, and B. Roulet: *J. Phys. (France)*, 1990, vol. 51, pp. 1847-64; B. Caroli, C. Caroli, and B. Roulet: *J. Phys. (France)*, 1990, vol. 51, pp. 1865-76.
13. Y.-J. Chen and S.H. Davis: *Acta Mater.*, 2001, vol. 49, pp. 1363-72.
14. S. Akamatsu and G. Faivre: *Phys. Rev. E*, 2000, vol. 61, pp. 3757-70.
15. G. Lesoult: *Ann. Chim. Fr.*, 1980, vol. 5, pp. 154-79, and references therein.
16. R. Trivedi, J.T. Mason, J.D. Verhoeven, and W. Kurz: *Metall. Trans. A*, 1991, vol. 22A, pp. 2523-33.
17. B. Caroli, C. Caroli, G. Faivre, and J. Mergny: *J. Cryst. Growth*, 1992, vol. 118, pp. 135-50.
18. S. Akamatsu, M. Plapp, G. Faivre, and A. Karma: *Phys. Rev. E*, 2002, vol. 66, 030501(R).
19. G. Dee and J.S. Langer: *Phys. Rev. Lett.*, 1983, vol. 50, pp. 383-86.
20. W. van Saarloos: in *Nonlinear Evolution of Spatio-Temporal Structures in Continuous Systems*, F.H. Busse and L. Kramer, eds., Plenum, New York, NY, 1990, pp. 499-508.
21. J.W. Cahn and J.E. Hilliard: *J. Chem. Phys.*, 1958, vol. 28, pp. 258-70.
22. R.A.L. Jones, L.J. Norton, E.J. Kramer, F.S. Bates, and P. Wiltzius: *Phys. Rev. Lett.*, 1991, vol. 66, pp. 1326-29; S. Puri and K. Binder: *Phys. Rev. E*, 1994, vol. 49, pp. 5359-77.
23. J. Mergny, G. Faivre, C. Guthmann, and R. Mellet: *J. Cryst. Growth*, 1993, vol. 134, pp. 353-68.
24. NIH Image is a public domain image processing and analysis program. It was developed at the Research Services Branch (RSB) of the National Institute of Mental Health (NIMH), part of the National Institutes of Health (NIH). It can be downloaded from <http://rsb.info.nih.gov/nih-image/download.html>
25. G. Faivre and J. Mergny: *Phys. Rev. A*, 1992, vol. 45, pp. 7320-29; *Phys. Rev. A*, 1992, vol. 46, pp. 963-72.
26. A. Karma: *Phys. Rev. E*, 1994, vol. 49, pp. 2245-50.
27. K.R. Elder, F. Drolet, J.M. Kosterlitz, and M. Grant: *Phys. Rev. Lett.*, 1994, vol. 72, pp. 6705-20.
28. M. Plapp and A. Karma: *Phys. Rev. E*, 2002, vol. 66, 061608.
29. M. Gündüz and J.D. Hunt: *Acta Metall.*, 1985, vol. 33, pp. 1651-72.
30. W.J. Boettinger: *Metall. Trans.*, 1974, vol. 5, pp. 2023-31.
31. M. Vandyoussefi, H.W. Kerr, and W. Kurz: *Acta Mater.*, 1997, vol. 45, pp. 4093-105; S. Dobler, T.S. Lo, M. Plapp, A. Karma and W. Kurz: *Acta Mater.*, in press (2004).